

# Efficient AI-Driven Multi-Section Whole Slide Image Analysis for Biochemical Recurrence Prediction in Prostate Cancer

Yesung Cho, Dongmyung Shin, Sujeong Hong, Jooyeon Lee, Seongmin Park, Geongyu Lee, Jongbae Park, and Hong Koo Ha

**Abstract**— Prostate cancer is one of the most frequently diagnosed malignancies in men worldwide. However, precise prediction of biochemical recurrence (BCR) after radical prostatectomy remains challenging due to the multifocality of tumors distributed throughout the prostate gland. In this paper, we propose a novel AI framework that simultaneously processes a series of multi-section pathology slides to capture the comprehensive tumor landscape across the entire prostate gland. To develop this predictive AI model, we curated a large-scale dataset of 23,451 slides from 789 patients. The proposed framework demonstrated strong predictive performance for 1- and 2-year BCR prediction, substantially outperforming established clinical benchmarks. The AI-derived risk score was validated as the most potent independent prognostic factor in a multivariable Cox proportional hazards analysis, surpassing conventional clinical markers such as pre-operative PSA and Gleason score. Furthermore, we demonstrated that integrating patch and slide sub-sampling strategies significantly reduces computational cost during both training and inference without compromising predictive performance, and generalizability of AI was confirmed through external validation. Collectively, these results highlight the clinical feasibility and prognostic value of the proposed AI-based multi-section slide analysis as a scalable tool for post-operative management in prostate cancer.

**Index Terms**— Biochemical recurrence prediction, Computational pathology, Multi-section whole-slide imaging, Deep multiple instance learning, Prognostic risk stratification

## I. INTRODUCTION

PROSTATE cancer remains one of the most prevalent cancers in men worldwide, with millions of new diagnoses annually [1], [2]. Primary treatments often involve radical prostatectomy (RP) or radiotherapy combined with androgen deprivation therapy, depending on cancer stage and patient health [3], [4], [5], [6]. However, even after treatment, a substantial proportion of patients experience biochemical recurrence (BCR), characterized by elevated

serum levels of prostate-specific antigen (PSA) [7], [8]. Therefore, there has been an increasing demand to predict the BCR outcomes of patients to guide the patient's treatment strategy, including the scheduling of surveillance intervals and the administration of adjuvant therapies [9], [10], [11]. Predicting early BCR is particularly important, as short-term recurrence strongly correlates with accelerated disease progression, elevated metastatic risk, and the eventual development of castration-resistant prostate cancer [12].

Previous studies have proposed many promising methods to stratify patient's risks of BCR based on clinical and/or pathological features [11], [13], [14], [15]. One of the well-known methods is Han Tables [15], which calculates the probability of BCR for up to 10 years using the PSA level, Gleason score, and pathological cancer stage. Furthermore, CAPRA-S [13] integrates additional information, such as surgical margin status and lymphatic invasion, for patient stratification [13], [16], [17]. Similarly, Bergero et al. [17] developed a new strategy to accurately predict future risks of BCR using a combinations of 16 clinical and pathological factors.

More recently, with the emergence of artificial intelligence (AI), computational pathology has been applied to BCR prediction [18]. For example, Cao et al. [19] developed a deep learning framework to predict the risk of BCR based on histology images of biopsy samples. Also, Huang et al. [20] introduced an AI model that analyzes whole slide images (WSIs) of prostate tissues to identify prognostic features related to BCR.

However, all previous works are restricted to single-region analysis, relying on an individual TMA core [21], [22], [23], biopsy [19], [24], or WSI from RP [20], [25] for each patient, which creates a spatially fragmented view that neglects the *multifocality* of prostate cancer [8], [26]. Unlike other malignancies, prostate cancer manifests as distinct tumor foci with heterogeneous characteristics distributed throughout the prostate gland [8], [9]. Therefore, precise BCR prediction necessitates specialized techniques capable of integrating features from these spatially distributed tumor regions. To

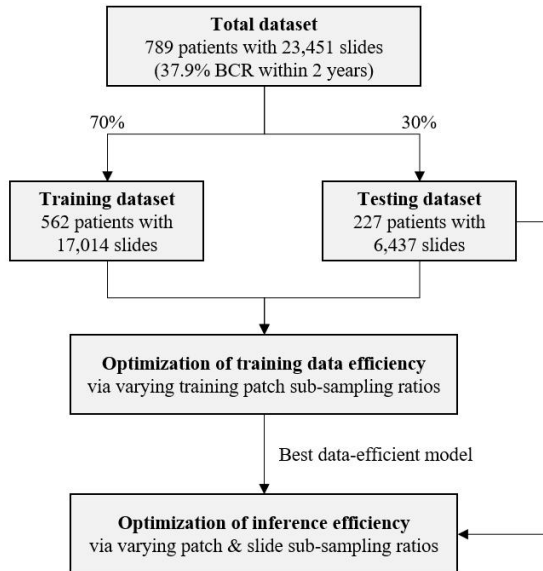
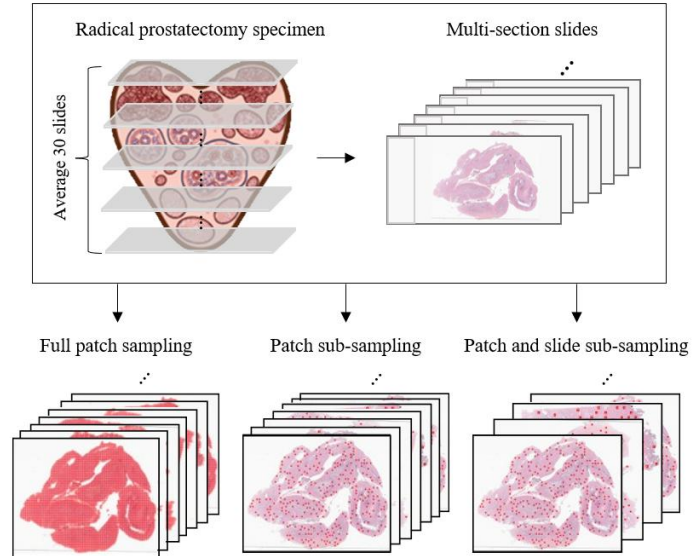
This work was supported in part by the Pusan National University. (Yesung Cho and Dongmyung Shin contributed equally to this work.) (Corresponding author: Jongbae Park and Hong Koo Ha).

Yesung Cho, Dongmyung Shin, Sujeong Hong, and Geongyu Lee are with the OmixAI Co. Ltd., Republic of Korea, 02636.

Dongmyung Shin and Sungmin Park are with the Oncocross Co. Ltd., Republic of Korea, 05836.

Jongbae Park is with the Department of Medicine, School of Medicine, Kyunghee University, Republic of Korea, 02447 (email: jbp@khu.ac.kr)

Jooyeon Lee and Hong Koo Ha is with the Department of Urology, School of Medicine, Pusan National University, Republic of Korea, 50612 (email: hongkooaha@pusan.ac.kr)

**(a) Overview of the study design and data pipeline****(b) Sampling strategies for multi-section slides**

**Fig. 1.** (a) Overview of the study design. The total data was partitioned into training and testing datasets with a 7:3 ratio. Then, AI performance was evaluated by varying training patch sub-sampling ratios to identify the best data-efficient model. This model was subsequently used to evaluate inference efficiency, assessing the trade-off between inference speed and predictive accuracy by varying patch and slide sub-sampling ratios in the test cohort. (b) Comparison of sampling schemes. Full patch sampling processes all extracted patches, leading to a prohibitive computational burden. Patch sub-sampling selectively retains an informative subset of patches based on tissue density. Slide sub-sampling selects a subset of multi-section slides to further reduce computational cost.

overcome these limitations, we propose a novel AI that simultaneously processes a series of multi-section WSIs of prostate glands for BCR prediction. This framework is designed to extract and integrate prognostic pathological features across the entire prostate gland, while substantially reducing computational demands for AI training and testing through patch and slide sub-sampling strategies. To develop this, we have curated 23,451 WSIs from 789 patient’s tissues after RP.

Our contributions are as follows:

- Development of a new AI framework that efficiently processes multi-section WSIs to extract and integrate prognostic features throughout the entire prostate gland, leveraging a large-scale, carefully curated dataset.
- Validation of the AI-derived risk score as a robust and independent prognostic marker for BCR-free survival, outperforming conventional clinical/pathological factors in a multivariable Cox proportional hazards analysis.
- Optimization of computational cost via patch and slide sub-sampling strategies, significantly accelerating both training and inference efficiency without compromising predictive performance.

## II. MATERIALS AND METHODS

### A. Patient Population and Characteristics

Multi-section WSIs derived from RP specimens were

retrospectively collected from Pusan National University between February 2010 and May 2025. The cohort included 789 patients (mean age:  $66.7 \pm 6.0$  years), with 299 (37.9 %) experiencing BCR within two years (mean time to BCR:  $6.98 \pm 6.6$  months) and 490 remaining BCR-free until then. The dataset consisted of a total of 23,451 slides, with an average of 29.7 slides per patient. For model training and evaluation, the cohort was randomly partitioned into a development set ( $n = 562$ ) and a test set ( $n = 227$ ) at a 7:3 ratio (see Fig. 1a).

In addition to BCR outcomes, several clinical/pathological variables were collected for each patient, including pre-operative PSA pathological stage, Gleason score, surgical margin status, lymphatic invasion, tumor percentage and number of positive lymph node. Detailed information for all the variables and their statistics is provided in Supplementary Table 1. The pathological parameters were assessed by a board-certified pathologist in the hospital.

In addition to the privately collected dataset, we utilized the publicly available CHIMERA dataset for external validation [27]. We used a cohort which comprised a total of 89 patients, where 21 patients (23.5%) experienced BCR within 2 years and others remained BCR-free until then.

### B. AI Model Training using Density-Based Patch Sampling

For AI development, we adopted an attention-based deep multiple instance learning (MIL) framework [28], using non-overlapping WSI patches with patient-level labels (i.e., BCR

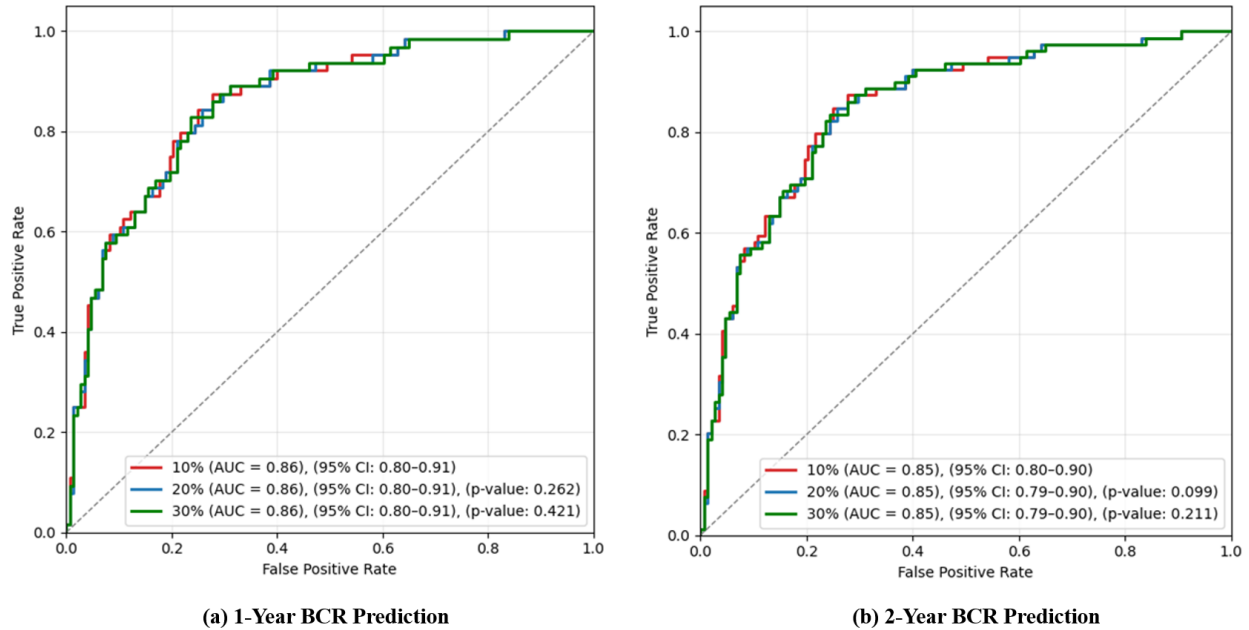


**Fig. 2.** Impact of training patch sub-sampling ratios on AI predictive performance. The ROC curves are shown for three ensemble models trained with 10%, 20%, and 30% sampling ratios within 1 year (a) and 2 years (b) in the test set ( $n=227$ ). The predictive performance across different sampling ratios are equivalent (0.85 or 0.86). Pairwise statistical comparisons using DeLong's test confirm no significant differences in AUC values between the 10% sampling model and the other models with higher ratios ( $p > 0.05$ ).

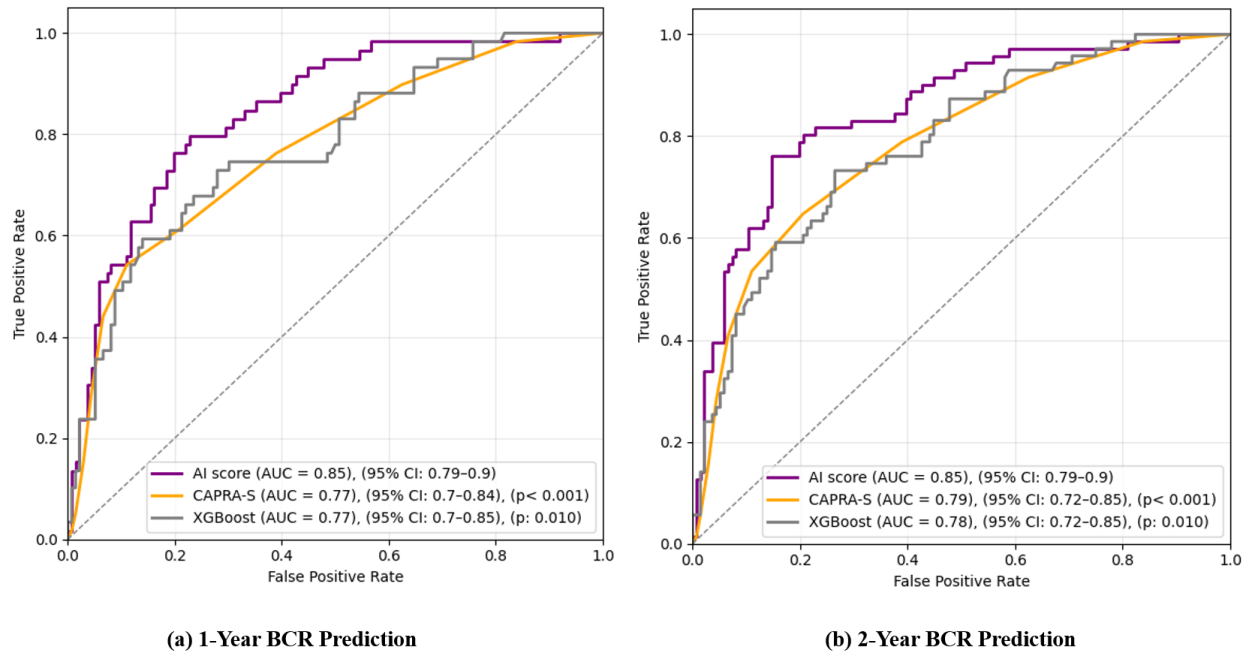


**Fig. 3.** ROC curves comparing the predictive performance of the AI score, CAPRA-S [13], and XGBoost model [17] for 1-year (a) and 2-year (b) BCR. At both time points, the AI model achieved superior predictive performance ( $= 0.85$ ), significantly outperforming CAPRA-S and XGBoost model ( $p < 0.05$ ). Note that 20 patients from the original test cohort were excluded from this analysis due to missing values in certain clinical variables.

outcome). Typically, standard WSI datasets represent a patient with a few WSI, allowing the use of all patches for AI training without significant computational burden. However, the dataset used in this study consists of multi-section WSIs covering the entire prostate gland. Therefore, utilizing every patch for training is computationally prohibitive, as the average slide

count per patient is 29.7 (see 'Full patch sampling' in Fig. 1b). To address this tremendous computational cost, we employed a patch sub-sampling method based on tissue density [29]. This sampling strategy prioritizes tissue-dense regions, thereby increasing the likelihood of selecting morphologically informative areas, while substantially reducing the patch count

compared to the full patch sampling strategy (see ‘Patch sub-sampling’ in Fig. 1b).

Let  $x_i \in R^2$  denote the center coordinate of the  $i^{th}$  patch, and  $N$  denote the total number of patches in a WSI. Then we estimate the sampling probability of the  $i^{th}$  patch ( $p_i$ ) as follows:

$$p_i = \frac{\hat{f}(x_i)}{\sum_{j=1}^N \hat{f}(x_j)}, \text{ where } \hat{f}(x) = \frac{1}{Nh^2} \sum_{k=1}^N K\left(\frac{x-x_k}{h}\right) \quad (1)$$

Here,  $K(\cdot)$  is a gaussian kernel function, and  $h$  denotes the bandwidth set to the patch size ( $= 512$ ). The term  $\hat{f}(x)$  represents the estimated patch density. By normalizing these density values, we derive the probability distribution  $\{p_i\}_{i=1}^N$  of individual patches. Based on these probabilities, we sampled a fixed fraction of patches per slide.

### C. Optimization of Training Data Efficiency with Varying Patch Sub-Sampling Ratios

First, we assessed the AI model’s predictive performance across different training patch sub-sampling ratios (10%, 20%, and 30%; see ‘Optimization of training data efficiency’ in Fig. 1a). For each ratio, five models were trained using a 5-fold cross-validation scheme in the development cohort ( $n = 562$ ). The predictions in the independent test cohort ( $n = 227$ ) were then generated using an ensemble approach, averaging the probability scores of the five cross-validated models. To ensure a fair comparison of predictive performance across different training patch sub-sampling ratios, inference was consistently performed using full patch sampling. These predictions were analyzed separately for 1-year and 2-year BCR. Performance was quantified using the area under the receiver operating characteristic curve (AUC) with 95% confidence intervals (CI) calculated by the bootstrap method with 2,000 iterations. Statistical significance ( $p < 0.05$ ) of the difference between the AUCs of the ensemble models was assessed using DeLong’s test [30]. The ensemble model with the best data efficiency was selected for subsequent experiments (see ‘Best data-efficient model’ in Fig. 1a).

### D. Comparison of Predictive Performance of AI with Other Clinical Models

We compared the predictive performance of the best data-efficient AI model with the CAPRA-S [13] and XGBoost model [17] for both 1-year and 2-year BCR. For XGBoost, we trained the model using the same hyperparameters (max depth=2, eta=0.2, rounds=23) reported in Bergero et al. [17]. However, due to differences in data availability, we could utilize 9 out of 16 clinical/pathological features used in the original study (see Supplementary Table 2). Specifically, among the 227 patients in the test set, 20 patients had missing data for some of these 9 clinical variables. Therefore, we additionally excluded these patients from the original test set, resulting in a total of 207 patients (BCR: 136; non-BCR: 71) for the comparative evaluation.

### E. Prognostic Evaluation: Multivariable Cox Regression and Risk Stratification

To evaluate the independent prognostic value of AI prediction for 2-year BCR adjusting for other confounding factors, we performed a multivariable Cox proportional hazards regression analysis [31]. The multivariable analysis incorporated the AI risk score (i.e., probabilistic outcome of BCR) alongside clinical/pathological variables, including age, pre-operative PSA, pathological T stage, Gleason score, surgical margin status, lymphatic invasion, tumor percentage and positive lymph node counts. We reported the hazard ratio (HR) with 95% CI for each variable with a Harrel’s concordance index (C-index). Statistical significance for individual variables was assessed using the Wald test [32]. Kaplan–Meier survival analysis for recurrence-free survival also performed with log-rank testing, where low- and high-risk groups were partitioned based on the median AI risk score derived from the training cohort.

### F. Optimization of Inference Efficiency with Varying Patch and Slide Sub-Sampling Ratios

To optimize inference efficiency of AI, we evaluated the trade-off between inference time and predictive accuracy for 2-year BCR across varying patch and slide sub-sampling ratios (see ‘Optimization of inference efficiency’ in Fig. 1a). First, we systematically varied the inference patch sub sampling ratio from 0.05% to 30% while recording both predictive performance (in AUC) and average inference time per patient (in minutes). The same density-based sampling method [29] employed during training was utilized for inference. Second, to quantify the impact of spatial coverage of slides on predictive accuracy, we incrementally added the number of inference slides, while keeping the inference patch sub-sampling ratio fixed (see ‘Patch and slide sub-sampling’ in Fig. 1b). We compared two slide-selection strategies: random sampling, where slides were selected arbitrarily, and uniform sampling, which selected the slides in equidistant intervals to maximize anatomical coverage. For both strategies, we produced performance curves, plotting AUC and average inference time per patient against the number of input slides.

### G. External Validation of AI Model

The generalizability of the trained AI model was assessed using the external CHIMERA dataset. We evaluated the robustness of the model by measuring its predictive power for both 1-year and 2-year BCR endpoints, reporting both the AUC and C-index. In addition, to check the transferability of the risk stratification, the median AI risk score derived from the internal training cohort was applied to this external data to classify patients into low-risk and high-risk groups. Kaplan–Meier survival analysis was subsequently performed to compare recurrence-free survival across these groups, confirming whether the AI score maintains its discriminative power and

TABLE I  
RESULTS OF MULTIVARIABLE COX PROPORTIONAL HAZARDS ANALYSIS

Variables	Coefficient $\beta$	Hazard Ratio (95% CI)	P-value	Significance
Preoperative PSA	0.01	1.01 (CI: 1.00 – 1.02)	0.009	**
Pathological Gleason Score	0.14	1.16 (CI: 1.02 – 1.31)	0.025	*
Surgical Margin Status	0.26	1.30 (CI: 1.07 – 1.59)	0.009	**
Tumor Percentage	0.003	1.00 (CI: 1.00 – 1.01)	0.124	
Positive Lymph Node Count	-0.002	1.00 (CI: 0.75 – 1.32)	0.987	
Age	0.001	1.00 (CI: 0.99 – 1.02)	0.860	
Pathological T stage				
2b	-0.36	0.70 (CI: 0.13 – 3.74)	0.672	
2c	-0.12	0.89 (CI: 0.73 – 1.09)	0.252	
3a	0.02	1.02 (CI: 0.81 – 1.28)	0.880	
3b	0.25	1.28 (CI: 1.00 – 1.64)	0.050	*
4	0.14	1.15 (CI: 0.46 – 2.89)	0.763	
Lymphatic Invasion	0.22	1.25 (CI: 0.97 – 1.62)	0.091	.
AI Risk Score	<b>1.38</b>	<b>3.97 (CI: 2.68 – 5.87)</b>	<b>p &lt; 0.001</b>	<b>***</b>
Evaluation Metrics	Values			
C-index	<b>0.79</b>			
. p < 0.1, * p < 0.05, ** < 0.01, *** p < 0.001				

prognostic validity in an independent cohort.

#### H. Implementation Details

For AI training and testing, non-overlapping patches of size  $512 \times 512$  were extracted at  $40\times$  magnification. Patch-level feature extraction was performed using the UNI foundation model [33]. These features served as input to the attention-based MIL framework [28]. The model architecture concludes with two output branches (BCR and non-BCR), where the final prediction is determined by the class with the higher probability. For model weight optimization, gradients accumulated over 16 iterations, with each iteration processing a batch of patches sampled from a single patient. An Adam optimizer was used with a learning rate of  $5 \times 10^{-6}$  and weight decay of  $5 \times 10^{-7}$ . The dropout rate was set to 0.25. All experiments were conducted on a workstation equipped with an Intel Xeon E5-2698 v4 CPU and four NVIDIA Tesla V100 GPUs (32GB VRAM).

### III. RESULTS

#### A. Optimization of Training Data Efficiency with Varying Patch Sub-Sampling Ratios

Figure 2 presents the model's predictive performance for 1- and 2-year BCR across varying training patch sub-sampling ratios (10%, 20%, and 30%). Notably, the model maintained consistent performance regardless of the sampling ratio, yielding AUCs of 0.86 and 0.85 for the 1-year (Fig. 2a) and 2-year (Fig. 2b) endpoints, respectively. Pairwise statistical analyses revealed no significant differences in predictive accuracy between the 10% sub-sampling model and those trained with higher ratios ( $p > 0.05$  for all comparisons). Because increasing the sampling ratio to 20% or 30%

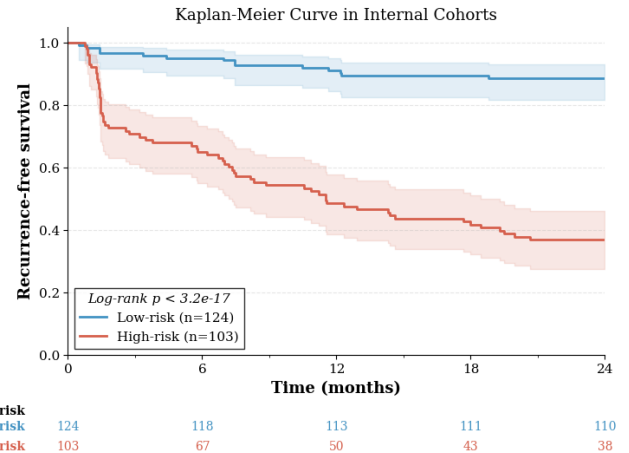


Fig. 4. Kaplan–Meier curve for recurrence-free survival in the internal test cohort ( $n = 227$ ), stratified by the AI-derived risk score. Patients were dichotomized into low-risk ( $n = 124$ ) and high-risk ( $n = 103$ ) groups using the median risk score determined from the training cohort. Shaded regions represent 95% confidence intervals.

provided no additional performance gains, the 10% ratio was selected as the best data-efficient model which maintains predictive accuracy while minimizing training cost.

#### B. Comparison of Predictive Performance of AI with Other Clinical Models

Predictive performance for 1-year and 2-year BCR was comparatively analyzed between our AI model and existing clinical models. For the 1-year endpoint, the AI model achieved a superior AUC of 0.85, compared to 0.77 for CAPRA-S and 0.77 for XGBoost. Similarly, for the 2-year endpoint, the AI model reported an AUC of 0.85, surpassing AUCs of CAPRA-S (= 0.79) and XGBoost (= 0.78). All the comparisons were statistically significant against both baselines ( $p < 0.05$ ). Consequently, these results demonstrate that our multi-section

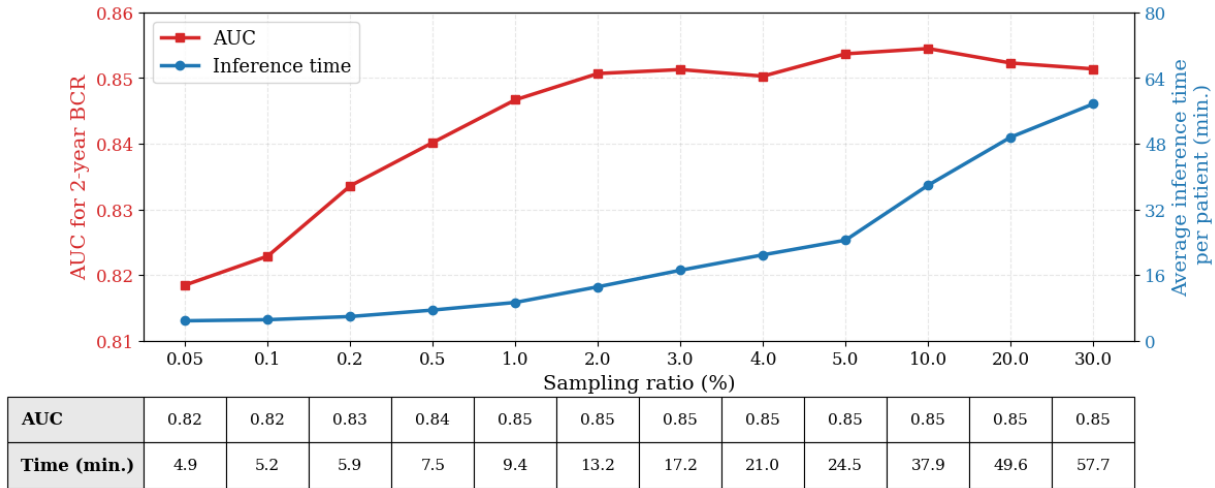


Fig. 5. Trade-off between predictive performance and inference time across varying inference patch sampling ratios. The graphs illustrate 2-year BCR predictive performance (AUC) and inference time (minutes) as the sampling ratio increases from 0.05% to 30%. The model retains substantial predictive power (AUC = 0.82) even at a minimal 0.05% ratio. An optimal balance is achieved at a 1% sampling ratio, which reaches peak performance (AUC = 0.85) with an inference time of 9.4 minutes, demonstrating that exhaustive patch sampling is unnecessary.

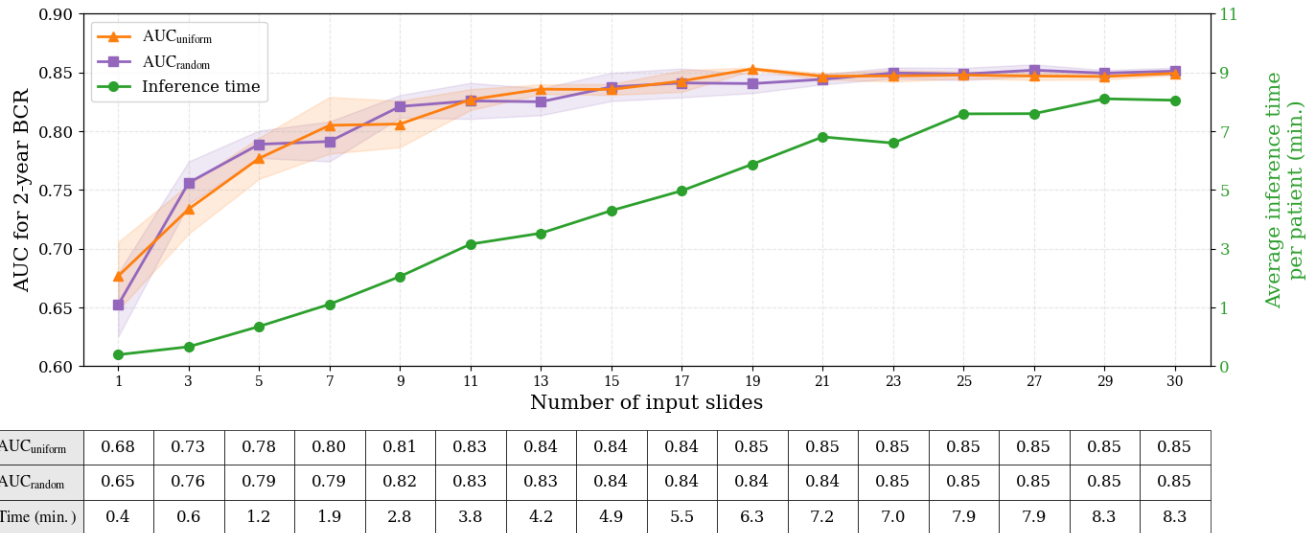


Fig. 6. Effect of slide-level sampling strategies on predictive performance and inference speed. The graphs compare uniform and random slide sampling strategies, depicting a steady increase in AUC that plateaus at 19 and 23 slides, respectively. The uniform sampling strategy optimally captures prognostic information, achieving peak accuracy (AUC = 0.85) using a representative subset of just 19 slides. This sampling point reduces the average inference time to 6.3 minutes per patient without compromising predictive accuracy.

pathology-based AI approach yields a stronger prognostic impact than models relying on traditional clinical/pathological factors.

### C. Prognostic Value of AI Risk Score: Multivariable Cox Regression and Kaplan-Meier Analysis

Table 1 presents the results of the multivariable Cox proportional hazards analysis to evaluate the prognostic value of the AI-derived risk score in conjunction with clinical/pathological variables for 2-year BCR. The analysis identified the AI risk score as the most potent and statistically significant predictor of BCR, with a hazard ratio (HR) of 3.97 ( $p < 0.001$ ), outperforming other established markers. In addition, the preoperative PSA (HR: 1.01,  $p = 0.009$ ) and Gleason score (HR: 1.16,  $p = 0.025$ ), and surgical margin status

(HR: 1.30,  $p = 0.009$ ) also showed significance. Overall, the predictive model demonstrated strong discriminatory ability, achieving a Concordance Index (C-index) of 0.79.

The risk stratification capability of the AI score was further validated using Kaplan–Meier survival analysis (Fig. 4). Within the internal test cohort ( $n = 227$ ), the AI score effectively stratified patients into distinct prognostic categories. The low-risk group ( $n = 124$ ) maintained a high recurrence-free survival rate of approximately 88% at 24 months. In contrast, the high-risk group ( $n = 103$ ) exhibited a substantially lower survival rate of roughly 37% at the same time point (log-rank  $p < 3.2 \times 10^{-17}$ ). This pronounced prognostic separation confirms the clinical utility of the AI risk score as a robust binary stratification tool for identifying patients at an elevated risk of BCR.

TABLE II  
PERFORMANCE METRICS (AUC AND C-INDEX) OF THE AI  
MODEL ON THE EXTERNAL VALIDATION CHIMERA DATASET FOR  
BIOCHEMICAL RECURRENCE (BCR) PREDICTION WITHIN 1 AND 2  
YEARS

Performance (100%	AUC (95% CI)	C-index
BCR within 1 year	0.79 (0.64 – 0.90)	0.78
BCR within 2 year	0.77 (0.64 – 0.90)	0.76

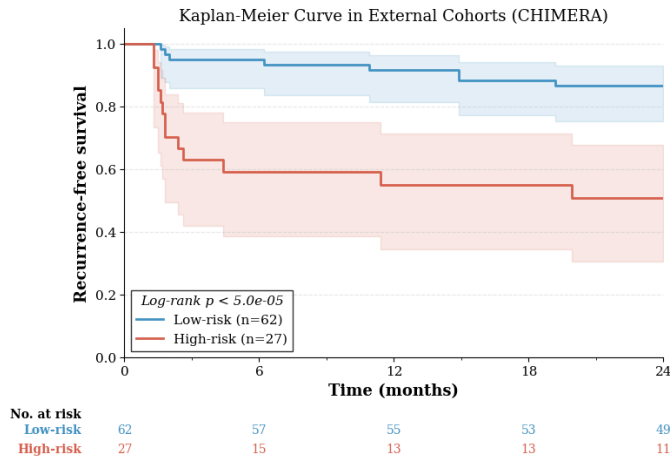


Fig. 7. Kaplan–Meier curves for recurrence-free survival in the external validation cohort (CHIMERA,  $n = 89$ ), stratified by the AI-derived risk score. The median AI risk score derived from the internal training cohort was applied to dichotomize patients into low-risk ( $n = 62$ ) and high-risk ( $n = 27$ ) groups. Shaded regions represent 95% confidence intervals.

#### D. Optimization of Inference Efficiency with Varying Patch and Slide Sub-Sampling Ratios

Figure 5 illustrates the trade-off between 2-year BCR predictive performance (in AUC) and inference time (in minutes) across varying inference patch sampling ratios. The AUC improved from 0.82 to 0.85 as the sampling ratio increased from 0.05% to 30%. Interestingly, the model retained substantial predictive power even at a minimal sampling ratio of 0.05% (AUC = 0.82), suggesting that most prognostic features are driven by a tiny fraction of highly informative patches. Inference time scaled with sampling ratios, requiring 9.4 and 13.2 minutes at 1% and 2% ratios, respectively. These results indicate that exhaustive patch sampling of multi-section slides during inference is unnecessary, and, consequently, a sampling of 1% is optimal to achieve peak performance (AUC = 0.85) with substantially reduced computational overhead.

Building upon our patch-level inference efficiency optimization, we investigated the effect of slide-level coverage on both predictive performance and inference speed. As depicted in Figure 6, both uniform and random slide sampling strategies exhibited a steady increase in AUC, peaking at 19 and 23 slides, respectively, before plateauing. Notably, the uniform sampling strategy achieved an AUC of 0.85 using only 19 slides, which consequently reduced the average inference time per patient to 6.3 minutes. These findings demonstrate that a representative subset of 19 evenly sampled slides adequately captures the prognostic information of the full multi-section

slide set, substantially alleviating the computational burden without compromising predictive accuracy.

#### E. External Validation of AI Model

Table 2 summarizes the external validation results of the AI model evaluated on the CHIMERA dataset. For 1-year BCR predictions, the model achieved an AUC of 0.79 and a C-index of 0.78. Similarly, for 2-year predictions, it yielded an AUC of 0.77 and a C-index of 0.76. While these metrics demonstrate robust generalizability, they reflect a marginal reduction in performance compared to the internal validation cohort (e.g., AUC of 0.86 vs. 0.79 for 1-year BCR). This is possibly attributed to the CHIMERA dataset comprising only partial tissue sections per patient (see Discussion).

To evaluate the model's capacity for risk stratification, a Kaplan-Meier survival analysis was also shown in Fig. 7. The AI-derived risk score successfully maintained significant stratification between patient cohorts. At 24 months, the low-risk group ( $n = 62$ ) exhibited a recurrence-free survival rate of approximately 86%, whereas the high-risk group ( $n = 27$ ) demonstrated a markedly lower survival rate of approximately 52% (log-rank  $p < 5.0 \times 10^{-5}$ ).

## IV. DISCUSSION

In this study, we developed an AI framework that simultaneously processes multi-section WSIs from RP specimens to predict BCR within 2 years. The proposed approach significantly outperformed established clinical benchmarks and was validated as the most potent independent prognostic factor in multivariable Cox regression analysis (Table 1).

The clinical significance of a 2-year recurrence endpoint is well-established in the literature. For instance, Freeland et al. [12] demonstrated that early biochemical recurrence following surgical is associated with adverse oncologic trajectories, indicating that the time to recurrence serves as a proxy for underlying disease aggressiveness. Corroborating studies [34], [35], [36] further establish that rapid biochemical progression is indicative of an aggressive tumor biology and correlates with poor downstream prognoses. Consequently, the accurate identification of patients at risk for recurrence within this 2-year window is critical for optimizing post-operative surveillance protocols and facilitating timely adjuvant therapies.

A central premise of this work is that comprehensive spatial coverage of the prostate gland provides prognostic information beyond what single-region analyses can capture. The consistent performance improvement from a single slide (AUC = 0.68) to 19 or more (AUC = 0.85), as shown in Fig. 6, provides direct empirical support. This aligns with the well-established tumor heterogeneity across prostate glands [8], [26] and suggests that multifocal features carry complementary prognostic signals lost when only a single section is examined.

The clinical relevance of accurate early BCR prediction is substantial. Current guidelines [3], [11] recommend discussing

salvage radiotherapy with patients exhibiting adverse pathological features, as timely intervention improves outcomes [9], [10]. However, not all such patients will experience BCR, and unnecessary treatment exposes patients to avoidable morbidity. Our AI-derived risk score, which demonstrated clear separation between low-risk (88% recurrence-free survival at 24 months) and high-risk (37% at 24 months) groups (Fig. 4), could help clinicians identify patients who would most benefit from intensified surveillance or early adjuvant therapy, while sparing low-risk patients from unnecessary interventions.

Computational efficiency is a prerequisite for clinical translation. Processing whole multi-section slides (average 29.7 slides per patient) with full patch sampling requires approximately 58 minutes processing time (Fig. 5). Our patch and slide sub-sampling strategy substantially mitigate this: reducing the patch sampling ratio to 1% preserved predictive performance (AUC = 0.85) at 9.4 minutes per patient, and further slide sub-sampling achieved equivalent performance with as few as 19 slides in approximately 6.3 minutes (Fig. 6). Ultimately, this streamlined processing time demonstrates the practical feasibility of integrating our model into routine clinical workflows.

A notable limitation of the CHIMERA dataset is its sparse representation of the prostate gland, averaging only 1.9 slides per patient. We hypothesize that this limited slide coverage is insufficient to adequately capture the inherent multifocality of prostate tumors, which likely accounts for the slight decrease in predictive performance observed during external validation (Table 2). Furthermore, the wider confidence intervals and the imbalanced risk group distribution (62 low-risk vs. 27 high-risk; Fig. 7) reflect the cohort's restricted sample size and divergent data characteristics compared to our internal dataset. However, despite these significant data constraints, the AI model maintained a strong C-index (0.78 and 0.76 for 1-year and 2-year BCR, respectively) and preserved its discriminative power on the external cohort. Collectively, these findings suggest that the proposed AI framework provides generalizable prognostic stratification for BCR prediction.

Several limitations should be acknowledged. First, the internal cohort was collected from a single institution, and although external validation on the CHIMERA dataset demonstrated generalizability, the cohort was limited (89 patients). Multi-institutional validation on larger cohorts is needed. Second, the framework employs a standard attention-based MIL [28] with the UNI [33] foundation model without considering inter-slide spatial relationships. Future work could explore hierarchical attention mechanisms to address this [37], [38], [39], [40]. In addition, incorporating prostate cancer-specific foundation models may further improve performance and robustness [41]. Third, comparison with prior methods was limited to a few clinical models. This is because existing pathology-based AI studies [19], [20], [21], [22] have not released their model weights for benchmarking, and notably, there is a lack of prior models designed to utilize multi-section whole slide images. Finally, integration of the AI risk score

with clinical variables in a combined model was not explored and may yield further improvements.

## V. CONCLUSION

In this study, we presented a computationally efficient AI framework that leverages multi-section WSIs to comprehensively capture the multifocality of prostate cancer for BCR prediction. The proposed framework achieved strong predictive performance for both 1-year (AUC = 0.86) and 2-year (AUC = 0.85) BCR prediction, substantially outperforming established clinical benchmarks. In multivariable Cox proportional hazards analysis, the AI-derived risk score emerged as the most potent independent prognostic factor (HR = 3.97,  $p < 0.001$ , C-index = 0.79), confirming its ability to stratify patient risk beyond conventional clinical and pathological variables. Moreover, our systematic evaluation of sub-sampling strategies demonstrated that inference with only 1% of available patches and as few as 19 slides preserved optimal predictive accuracy while substantially reducing computational cost. External validation further confirmed its potential generalizability on the CHIMERA dataset, yielding AUCs of 0.79 and 0.77 for 1- and 2-year BCR prediction, respectively. In conclusion, we demonstrated the clinical feasibility of this comprehensive multi-section WSI analysis as a scalable and actionable tool for guiding post-operative management in prostate cancer patients.

## ACKNOWLEDGEMENT

Approval for the use of the study data was granted by the Institutional Review Board (IRB No. 2202-006-110) of Pusan National University Hospital. Patient identifiers were permanently erased to guarantee that the subsequent analysis was conducted anonymously. This work was supported by the National Research Foundation of Korea(NRF) grant funded by the Korea government(MSIT). (No. NRF-2023R1A2C1003760)

## REFERENCES

- [1] N. I. Simon, C. Parker, T. A. Hope, and C. J. Paller, "Best approaches and updates for prostate cancer biochemical recurrence," *ASCO Educ. Book*, vol. 42, p. 1, 2022, doi: 10.1200/EDBK\_351033.
- [2] R. Tourinho-Barbosa, V. Srougi, I. Nunes-Silva, M. Baghdadi, G. Rembeye, S. S. Eifel, and R. Sanchez-Salas, "Biochemical recurrence after radical prostatectomy: what does it mean?" *Int. Braz. J. Urol.*, vol. 44, no. 1, pp. 14–21, Jan.–Feb. 2018, doi: 10.1590/S1677-5538.IBJU.2016.0656.
- [3] N. Mottet, R. C. van den Bergh, E. Briers, et al., "EAU-EANM-ESTRO-ESUR-SIOG guidelines on prostate cancer 2020 update. Part 1: screening, diagnosis, and local treatment with curative intent," *Eur. Urol.*, vol. 79, no. 2, pp. 243–262, Feb. 2021, doi: 10.1016/j.eururo.2020.09.042.
- [4] J. L. Mohler, E. S. Antonarakis, A. J. Armstrong, et al., "Prostate cancer, version 2.2019, NCCN clinical practice guidelines in oncology," *J. Natl. Compr. Canc. Netw.*, vol. 17, no. 5, pp. 479–505, May 2019, doi: 10.6004/jnccn.2019.0023M. Løv, S. Zhao, U. Axcrone, B. Johannessen, A. C. Bakken, K. T. Carm, and R. I. Skotheim, "Multifocal primary prostate cancer exhibits high degree of genomic heterogeneity," *Eur. Urol.*, vol. 75, no. 3, pp. 498–505, Mar. 2019, doi: 10.1016/j.eururo.2018.08.009.

- [5] A. V. D'Amico, R. Whittington, S. B. Malkowicz, et al., "Biochemical outcome after radical prostatectomy, external beam radiation therapy, or interstitial radiation therapy for clinically localized prostate cancer," *JAMA*, vol. 280, no. 11, pp. 969–974, Sep. 1998, doi: 10.1001/jama.280.11.969
- [6] Bill-Axelsson, L. Holmberg, H. Garmo, et al., "Radical prostatectomy or watchful waiting in prostate cancer 29-year follow-up," *N. Engl. J. Med.*, vol. 379, no. 24, pp. 2319–2329, Dec. 2018, doi: 10.1056/NEJMoa18078
- [7] S. U. Lee, J. S. Kim, Y. S. Kim, J. Cho, S. H. Choi, T. K. Nam, and K. H. Cho, "Optimal definition of biochemical recurrence in patients who receive salvage radiotherapy following radical prostatectomy for prostate cancer," *Cancer Res. Treat.*, vol. 54, no. 4, pp. 1191–1199, Oct. 2022, doi: 10.4143/crt.2021.985.
- [8] M. Lovf, S. Zhao, U. Axcrone, B. Johannessen, A. C. Bakken, K. T. Carm, and R. I. Skotheim, "Multifocal primary prostate cancer exhibits high degree of genomic heterogeneity," *Eur. Urol.*, vol. 75, no. 3, pp. 498–505, Mar. 2019, doi: 10.1016/j.eururo.2018.08.009.
- [9] I. M. Thompson, C. M. Tangen, J. Paradelo, et al., "Adjuvant radiotherapy for pathologically advanced prostate cancer: a randomized clinical trial," *JAMA*, vol. 296, no. 19, pp. 2329–2335, Nov. 2006, doi: 10.1001/jama.296.19.2329.
- [10] A. J. Stephenson, P. T. Scardino, M. W. Kattan, et al., "Predicting the outcome of salvage radiation therapy for recurrent prostate cancer after radical prostatectomy," *J. Clin. Oncol.*, vol. 25, no. 15, pp. 2035–2041, May 2007, doi: 10.1200/JCO.2006.08.9607.
- [11] T. M. Morgan, S. A. Boorjian, M. K. Buyyounouski, et al., "Salvage therapy for prostate cancer: AUA/ASTRO/SUO guideline part 1: introduction and treatment decision-making at the time of suspected biochemical recurrence after radical prostatectomy," *J. Urol.*, vol. 211, no. 4, pp. 509–517, Apr. 2024, doi: 10.1097/JU.0000000000003892
- [12] S. J. Freedland, E. B. Humphreys, L. A. Mangold, M. Eisenberger, F. J. Dorey, P. C. Walsh, and A. W. Partin, "Risk of prostate cancer-specific mortality following biochemical recurrence after radical prostatectomy," *JAMA*, vol. 294, no. 4, pp. 433–439, Jul. 2005, doi: 10.1001/jama.294.4.433.
- [13] M. R. Cooperberg, J. F. Hilton, and P. R. Carroll, "The CAPRA-S score: a straightforward tool for improved prediction of outcomes after radical prostatectomy," *Cancer*, vol. 117, no. 22, pp. 5039–5046, Nov. 2011, doi: 10.1002/cncr.26169.
- [14] A. J. Stephenson, P. T. Scardino, J. A. Eastham, et al., "Postoperative nomogram predicting the 10-year probability of prostate cancer recurrence after radical prostatectomy," *J. Clin. Oncol.*, vol. 23, no. 28, pp. 7005–7012, Oct. 2005, doi: 10.1200/JCO.2005.01.867.
- [15] M. Han, A. W. Partin, M. Zahurak, et al., "Biochemical (prostate specific antigen) recurrence probability following radical prostatectomy for clinically localized prostate cancer," *J. Urol.*, vol. 169, no. 2, pp. 517–523, Feb. 2003, doi: 10.1097/01.ju.0000045749.90353.c7.
- [16] V. Iremashvili, L. Pelaez, M. Jorda, D. J. Parekh, and S. Punnen, "A comprehensive analysis of the association between Gleason score at a positive surgical margin and the risk of biochemical recurrence after radical prostatectomy," *Am. J. Surg. Pathol.*, vol. 43, no. 3, pp. 369–373, Mar. 2019, doi: 10.1097/PAS.0000000000001204.
- [17] M. A. Bergero, P. Martinez, P. Modina, R. Hosman, W. Villamil, R. Gudiño, and L. Costa, "Artificial intelligence model for predicting early biochemical recurrence of prostate cancer after robotic-assisted radical prostatectomy," *Sci. Rep.*, vol. 15, no. 1, 2025, Art. no. 30822, doi: 10.1038/s41598-025-16362-1
- [18] M. S. Hosseini, B. E. Bejnordi, V. Q. H. Trinh, et al., "Computational pathology: a survey review and the way forward," *J. Pathol. Inform.*, vol. 15, Art. no. 100357, 2024, doi: 10.1016/j.jpi.2023.100357
- [19] L. Cao, R. He, A. Zhang, et al., "Development of a deep learning system for predicting biochemical recurrence in prostate cancer," *BMC Cancer*, vol. 25, Art. no. 232, 2025, doi: 10.1186/s12885-025-13628-9.
- [20] W. Huang, R. Randhawa, P. Jain, et al., "A novel artificial intelligence-powered method for prediction of early recurrence of prostate cancer after prostatectomy and cancer drivers," *JCO Clin. Cancer Inform.*, vol. 6, Art. no. e2100131, 2022, doi: 10.1200/JCOI.21.00131
- [21] H. Pinckaers, J. van Ipenburg, J. Melamed, et al., "Predicting biochemical recurrence of prostate cancer with artificial intelligence," *Commun. Med.*, vol. 2, Art. no. 64, 2022, doi: 10.1038/s43856-022-00126-3.
- [22] O. Eminaga, F. Saad, Z. Tian, U. Wolfgang, P. I. Karakiewicz, V. Ouellet, and S. R. Leyh-Bannurah, "Artificial intelligence unravels interpretable malignancy grades of prostate cancer on histology images," *npj Imaging*, vol. 2, no. 1, Art. no. 6, 2024, doi: 10.1038/s44303-023-00005-z.
- [23] M. Farrokh, N. Kumar, P. H. Gann, and R. Greiner, "Learning to predict prostate cancer recurrence from tissue images," *J. Pathol. Inform.*, vol. 15, Art. no. 100344, 2024, doi: 10.1016/j.jpi.2023.100344
- [24] M. Tsuneki, M. Abe, S. Ichihara, et al., "Inference of core needle biopsy whole slide images requiring definitive therapy for prostate cancer," *BMC Cancer*, vol. 23, Art. no. 11, 2023, doi: 10.1186/s12885-022-10488-5
- [25] T. Y. Kwak, C. H. Lee, W. Y. Park, J. Y. Ku, C. W. Jeong, E. C. Hwang, and H. K. Ha, "Clinical implications of deep learning based image analysis of whole radical prostatectomy specimens," *Sci. Rep.*, vol. 15, no. 1, Art. no. 11006, 2025, doi: 10.1038/s41598-025-95267-5
- [26] A. Erickson, A. Hayes, T. Rajakumar, C. Verrill, R. J. Bryant, F. C. Hamdy, and A. D. Lamb, "A systematic review of prostate cancer heterogeneity: understanding the clonal ancestry of multifocal disease," *Eur. Urol. Oncol.*, vol. 4, no. 3, pp. 358–369, Jun. 2021, doi: 10.1016/j.euo.2021.02.008
- [27] CHIMERA Organizers. (2025). Combined Histopathology and Imaging for Multi-modal Evaluation of Risk and Analytics Challenge. [Online]. Available: <https://chimera.grand-challenge.org/>
- [28] M. Ilse, J. Tomczak, and M. Welling, "Attention-based deep multiple instance learning," in *Proc. 35th Int. Conf. Mach. Learn. (ICML)*, Stockholm, Sweden, Jul. 2018, pp. 2127–2136.
- [29] S. Alfasly, A. Shafique, P. Nejat, J. Khan, A. Alsaafin, G. Alabtah, and H. R. Tizhoosh, "Rotation-agnostic image representation learning for digital pathology," in *Proc. IEEE/CVF Conf. Comput. Vis. Pattern Recognit. (CVPR)*, Seattle, WA, USA, 2024, pp. 11683–11693
- [30] E. R. DeLong, D. M. DeLong, and D. L. Clarke-Pearson, "Comparing the areas under two or more correlated receiver operating characteristic curves: a nonparametric approach," *Biometrics*, vol. 44, no. 3, pp. 837–845, Sep. 1988, doi: 10.2307/2531595
- [31] D. R. Cox, "Regression models and life-tables," *J. R. Stat. Soc. Ser. B Methodol.*, vol. 34, no. 2, pp. 187–202, 1972, doi: 10.1111/j.2517-6161.1972.tb00899.x
- [32] A. Wald, "Tests of statistical hypotheses concerning several parameters when the number of observations is large," *Trans. Am. Math. Soc.*, vol. 54, no. 3, pp. 426–482, Nov. 1943, doi: 10.1090/S0002-9947-1943-0012401-3
- [33] R. J. Chen, T. Ding, M. Y. Lu, D. F. Williamson, G. Jaume, A. H. Song, and F. Mahmood, "Towards a general-purpose foundation model for computational pathology," *Nat. Med.*, vol. 30, no. 3, pp. 850–862, Mar. 2024, doi: 10.1038/s41591-024-02857-3
- [34] D. M. Moreira, L. E. Howard, K. N. Sourbeer, H. S. Amarasekara, L. C. Chow, D. C. Cockrell, et al., "Predictors of time to metastasis in castration-resistant prostate cancer," *Urology*, vol. 96, pp. 171–176, Oct. 2016, doi: 10.1016/j.urology.2016.06.011.
- [35] L. E. Howard, D. M. Moreira, A. De Hoedt, W. J. Aronson, C. J. Kane, C. L. Amling, et al., "Thresholds for PSA doubling time in men with non metastatic castration-resistant prostate cancer," *BJU Int.*, vol. 120, no. 5B, pp. E80–E86, Nov. 2017, doi: 10.1111/bju.13856.
- [36] A. R. Metwalli, I. L. Rosner, J. Cullen, Y. Chen, T. Brand, S. A. Brassell, et al., "Elevated alkaline phosphatase velocity strongly predicts overall survival and the risk of bone metastases in castrate-resistant prostate cancer," *Urol. Oncol.*, vol. 32, no. 6, pp. 761–768, Aug. 2014, doi: 10.1016/j.urolonc.2014.03.024.
- [37] Z. Shao, Y. Chen, H. Bian, J. Zhang, G. Liu, and Y. Zhang, "HVTSurv: Hierarchical vision transformer for patient-level survival prediction from whole slide image," in *Proc. AAAI Conf. Artif. Intell.*, vol. 37, no. 2, 2023, pp. 2209–2217, doi: 10.1609/aaai.v37i2.25315
- [38] R. J. Chen, M. Y. Lu, M. Shaban, C. Chen, T. Y. Chen, D. F. Williamson, and F. Mahmood, "Whole slide images are 2D point clouds: Context aware survival prediction using patch-based graph convolutional networks," in *Proc. Med. Image Comput. Comput. Assist. Interv. (MICCAI)*, Strasbourg, France, 2021, pp. 339–349, doi: 10.1007/978-3-030-87237-3\_33
- [39] J. Song, Y. Hao, H. Zhai, S. Zhao, T. Ning, S. Huang, and X. Duan, "Multi-scale hierarchical context-aware survival prediction network based on whole slide images," *Biomed. Signal Process. Control*, vol. 107, Art. no. 107780, 2025, doi: 10.1016/j.bspc.2025.108159
- [40] P. Liu, L. Ji, F. Ye, and B. Fu, "Look a group at once: Multi-slide modeling for survival prediction," *arXiv preprint arXiv:2411.11487*, 2024, doi: 10.48550/arXiv.2411.11487
- [41] Y. Cho, S. Lee, G. Lee, M. Lee, J. Park, and D. Shin, "G2L: From Giga-Scale to Cancer-Specific Large-Scale Pathology Foundation Models via Knowledge Distillation," *arXiv preprint arXiv:2510.11176/* doi: 10.48550/arXiv.2510.11176

## Supplementary Material

Table S1. Clinical and pathological statistics of the study cohort. BCR: biochemical recurrence. PSA: prostate specific antigen. GS: Gleason score.

		Developing Dataset		Test Dataset	
		With BCR	Without BCR	With BCR	Without BCR
Number of Patients		220	342	79	148
Number of Slides		6,526	10,488	2,154	4,283
Age		66.42 ± 5.76	66.43 ± 6.23	66.91 ± 5.43	67.45 ± 6.09
Pre-operative PSA (ng/mL)		16.36 ± 16.06	8.72 ± 6.86	18.34 ± 22.32	9.54 ± 11.43
Tumor Percentage (%)		33.69 ± 24.54	16.65 ± 15.61	28.96 ± 23.54	14.60 ± 16.30
Pathological Stage					
	T1c	1 (0.5%)	0 (0.0%)	0 (0.0%)	0 (0.0%)
	T2a	16 (7.3%)	49 (14.3%)	10 (12.7%)	23 (15.5%)
	T2b	1 (0.5%)	2 (0.6%)	0 (0.0%)	0 (0.0%)
	T2c	66 (30.0%)	195 (57.0%)	30 (38.0%)	99 (66.9%)
	T3a	58 (26.4%)	68 (19.9%)	20 (25.3%)	19 (12.8%)
	T3b	74 (33.6%)	23 (6.7%)	17 (21.5%)	7 (4.7%)
	T4	3 (1.4%)	1 (0.3%)	0 (0.0%)	0 (0.0%)
	LN metastasis	3 (1.4%)	1 (0.3%)	0 (0.0%)	0 (0.0%)
	Unknown	1 (0.5%)	4 (1.2%)	2 (2.5%)	0 (0.0%)
Pathological Gleason Score					
	GS6	4 (1.8%)	73 (21.3%)	6 (7.6%)	54 (36.5%)
	GS7	154 (70.0%)	246 (71.9%)	48 (60.8%)	87 (58.8%)
	GS8	22 (10.0%)	12 (3.5%)	10 (12.7%)	2 (1.4%)
	GS9	36 (16.4%)	8 (2.3%)	13 (16.5%)	2 (1.4%)
	Unknown	4 (1.8%)	3 (0.9%)	2 (2.5%)	3 (2.0%)
Surgical Margin Status					
	Complete Resection	86 (39.1%)	259 (75.7%)	30 (38.0%)	107 (72.3%)
	Microscopic Residual Tumor	133 (60.5%)	81 (23.7%)	49 (62.0%)	41 (27.7%)
	Unknown	1 (0.5%)	2 (0.6%)	0 (0.0%)	0 (0.0%)
Lymphatic Invasion					
	Positive	51 (23.2%)	22 (6.4%)	13 (16.5%)	1 (0.7%)
	Negative	166 (75.5%)	315 (92.1%)	64 (81.0%)	147 (99.3%)
	Unknown/Equivocal	3 (1.4%)	5 (1.5%)	2 (2.5%)	0 (0.0%)
Positive Lymph Node Count					
	0	199 (90.5%)	316 (92.4%)	72 (91.1%)	137 (92.6%)
	1	9 (4.1%)	3 (0.9%)	1 (1.3%)	2 (1.4%)
	2	2 (0.9%)	1 (0.3%)	0 (0.0%)	0 (0.0%)
	5	1 (0.5%)	0 (0.0%)	0 (0.0%)	0 (0.0%)
	Unknown	9 (4.1%)	22 (6.4%)	6 (7.6%)	9 (6.1%)

Table S2. Clinical and pathological variables overlapped between Bergero et al [17] and our study.

Clinical/Pathological Variables	Bergero et al	Our study
Pathological Gleason Score	Used	Used
Prostate Capsule Infiltration	Used	Not used
Infiltration (mm)	Used	Not used
Surgical Margin Status	Used	Used
Lymphatic Invasion	Used	Used
Tumor Percentage	Used	Used
Pathological T stage	Used	Used
Age	Used	Used
Tumor Volume	Used	Not used
D'Amico Risk Groups	Used	Not used
PI-RADS	Used	Not used
Lymph Node Dissection	Used	Not used
Neurovascular Bundle Preservation	Used	Not used
Positive Lymph Node Count	Used	Used
Extraprostatic Disease	Used	Used
Pre-operative PSA	Used	Used